



ALMA Observations Reveal No Preferred Outflow-filament and Outflow-magnetic Field Orientations in Protoclusters

T. Baug¹, Ke Wang^{1,16}, Tie Liu², Mengyao Tang³, Qizhou Zhang⁴, Di Li^{5,6}, Chakali Eswaraiah^{5,7}, Sheng-Yuan Liu⁸, Anandmayee Tej⁹, Paul F. Goldsmith¹⁰, Leonardo Bronfman¹¹, Sheng-Li Qin³, Viktor L. Tóth¹², Pak-Shing Li¹³, and Kee-Tae Kim^{14,15}

¹ Kavli Institute for Astronomy and Astrophysics, Peking University, 5 Yiheyuan Road, Haidian District, Beijing 100871, People's Republic of China
kwang.astro@pku.edu.cn

² Shanghai Astronomical Observatory, Chinese Academy of Sciences, 80 Nandan Road, Shanghai 200030, People's Republic of China

³ Department of Astronomy, Yunnan University, Kunming, 650091, People's Republic of China

⁴ Center for Astrophysics | Harvard & Smithsonian, 60 Garden Street, Cambridge, MA 02138, USA

⁵ CAS Key Laboratory of FAST, National Astronomical Observatories, Chinese Academy of Sciences, Beijing 100101, People's Republic of China

⁶ University of Chinese Academy of Sciences, Beijing 100049, People's Republic of China

⁷ National Astronomical Observatories, Chinese Academy of Science, A20 Datun Road, Chaoyang District, Beijing 100012, People's Republic of China

⁸ Academia Sinica, Institute of Astronomy and Astrophysics, P.O. Box 23-141, Taipei 106, Taiwan

⁹ Indian Institute of Space Science and Technology, Thiruvananthapuram 695 547, Kerala, India

¹⁰ Jet Propulsion Laboratory, California Institute of Technology, USA

¹¹ Departamento de Astronomía, Universidad de Chile, Casilla 36-D, Santiago, Chile

¹² Eötvös Loránd University, Department of Astronomy, Pázmány Péter sétány 1/A, H-1117, Budapest, Hungary

¹³ Astronomy Department, University of California, Berkeley, USA

¹⁴ Korea Astronomy and Space Science Institute, 776 Daedeokdae-ro, Yuseong-gu, Daejeon 34055, Republic of Korea

¹⁵ University of Science and Technology, Korea (UST), 217 Gajeong-ro, Yuseong-gu, Daejeon 34113, Republic of Korea

Received 2019 October 6; revised 2019 December 23; accepted 2019 December 30; published 2020 February 11

Abstract

We present a statistical study of the orientation of outflows with respect to large-scale filaments and magnetic fields. Although filaments are widely observed toward Galactic star-forming regions, the exact role of filaments in star formation is unclear. Studies toward low-mass star-forming regions revealed both preferred and random orientations of outflows with respect to the filament long axes, while outflows in massive star-forming regions are mostly oriented perpendicular to the host filaments and parallel to the magnetic fields at similar physical scales. Here, we explore outflows in a sample of 11 protoclusters in H II regions, a more evolved stage compared to infrared dark clouds, using Atacama Large Millimeter/submillimeter Array CO (3–2) line observations. We identify a total of 105 outflow lobes in these protoclusters. Among the 11 targets, 7 are embedded within parsec-scale filamentary structures detected in ¹³CO line and 870 μ m continuum emissions. The angles between outflow axes and corresponding filaments (γ_{Fil}) do not show any hint of preferred orientations (i.e., orthogonal or parallel as inferred in numerical models) with respect to the position angle of the filaments. Identified outflow lobes are also not correlated with the magnetic fields and Galactic plane position angles. Outflows associated with filaments aligned along the large-scale magnetic fields are also randomly oriented. Our study presents the first statistical results of outflow orientation with respect to large-scale filaments and magnetic fields in evolved massive star-forming regions. The random distribution suggests a lack of alignment of outflows with filaments, which may be a result of the evolutionary stage of the clusters.

Unified Astronomy Thesaurus concepts: Star formation (1569); Submillimeter astronomy (1647); H II regions (694); Stellar jets (1607); Protoclusters (1297); Interstellar filaments (842); Interstellar medium (847)

1. Introduction

Herschel observations revealed ubiquitous filamentary structures in Galactic star-forming clouds. Filaments are observationally characterized as overdense elongated features of molecular clouds with an aspect ratio of more than ~ 5 –10 (André et al. 2014). These filaments are considered to play an important role in star formation. Dense star-forming cores may form within these filamentary structures (André et al. 2010; Arzoumanian et al. 2011; Lee et al. 2014). Filaments are even capable of leading the formation of massive stars ($m_* \gtrsim 8 M_\odot$) at their common junction (“hub;” Myers 2009; Dale & Bonnell 2011). Two types of gas flows are typically expected in a star-forming filament. These could be large-scale flows from the surrounding cloud onto the short-axis of the filament or the flow of gas from the parent cloud along the long axis of

the filament (Kirk et al. 2013; Fernández-López et al. 2014). Generally, the flow of gas along the long axis of a filament is implied by velocity gradients of the gas within filaments (Liu et al. 2016b; Wang 2018; Yuan et al. 2018). Observationally, such phenomena are indeed noted in several Galactic massive star-forming regions (e.g., Liu et al. 2012; Busquet et al. 2013; Baug et al. 2018; Lu et al. 2018; Yuan et al. 2018).

Classically, it is expected that the angular momentum of a star-forming molecular cloud is transported to protostars via dense cores (Bodenheimer 1995). In a non-turbulent scenario, the flow of gas along the short or long axes of a filament leads to rotation of the embedded cores either parallel or perpendicular to the parent filament. Under such conditions, if the embedded protostars within the cores inherit the angular momentum axis, they should also follow the same preferred direction of the rotation as the cores. However, numerical studies showed that the inflow of turbulent gas along a filament onto a core may affect the dynamics of the core and may even

¹⁶ Corresponding author.

lead to fragmentation (see Kudoh & Basu 2008; Offner et al. 2016, and references therein). It is also possible that the rotation axis of a protostar is independent of the natal filamentary structure. Even the angular momentum axes of cores were found to be distributed randomly regardless of the cloud or filamentary structures (see, e.g., Goodman et al. 1993; Tatematsu et al. 2016). The simulations of Offner et al. (2016) showed that the wide binary (>500 au) of slightly magnetically supercritical turbulent cores might also affect the rotation axis. Recently, Lee et al. (2016) found randomly aligned outflow axes (vis-a-vis rotation axes) of wide binary pairs.

A comprehensive method for understanding the influence of filaments on protostars would require identifying an explicit correlation between the protostellar accretion and gas flow along the filaments. But a direct detection of accreting gas at the core scale is difficult not only because of inadequate resolution and sensitivity of current observational facilities, but also because of the complicated gas dynamics at that scale. However, a solution to this problem could be a correlation between the protostellar jets or bipolar outflows associated with the filamentary structures. It is generally understood that these bipolar outflows are launched by the rotating accretion disk of the protostar, and can be used to infer the orientation of the rotation axis. Also, these outflows are much easier to detect and identify compared to accretion disks (Bally 2016, and references therein).

Recently, Stephens et al. (2017) explored the low-mass star-forming Perseus molecular cloud using Submillimeter Array observations and performed a statistical study of the orientation between outflows and filaments using a sample of 57 protostars. They found a random distribution of outflow-filament orientations. Outflow orientation studies in massive star-forming regions are comparatively limited only to a few regions. Wang et al. (2011) studied the P1 filament in IRDC G28.34+0.06 and found that outflows are orientated mostly perpendicular to the filament but parallel to parsec-scale magnetic fields. Kong et al. (2019) followed up the entire area of the same IRDC using the Atacama Large Millimeter/submillimeter Array (ALMA) data, and found a consistent result, i.e., the continuum sources that are situated on the parent filament typically have outflows directed perpendicular to the filament long axis.

Alongside the filaments, magnetic fields are also known to play a crucial role in star formation (Machida et al. 2005; Machida et al. 2020; Hull & Zhang 2019). In a recent study, Li & Klein (2019) showed the possibility of perpendicular alignment of momentum axis in the moderately strong magnetized filaments. On the other hand, Galametz et al. (2018) suggested a bimodal distribution of outflows with respect to the magnetic field orientation. Momentum axes perpendicular to the filament are indeed observed in parsec-scale clumps in the massive star-forming IRDC by Wang et al. (2011, 2012), and also at 0.1 pc scales in seven low-mass protostellar cores by Chapman et al. (2013). However, the majority of these studies found a contrasting result, like randomly oriented outflow axes with respect to parsec-scale magnetic fields (Targon et al. 2011). In a detailed observational study, Zhang et al. (2014) found that magnetic fields are dynamically important during the collapse of parsec-scale clumps and the formation of sub-parsec-scale cores. They also reported that the role of magnetic fields is less important than gravity and angular momentum from the core to the disk scale by comparing core magnetic fields with the outflow axis. In a study of low-mass star-forming cores,

Hull et al. (2014) also found a noncorrelation between outflow axis and envelope magnetic fields.

Most previous comprehensive studies are based on nearby low-mass star-forming regions, with a limited number of case studies on massive star-forming regions (Wang et al. 2011, 2012; Kong et al. 2019). In this paper, we study the outflows of 11 massive protoclusters ($1\text{--}24 \times 10^3 M_{\odot}$; Liu et al. 2016a) using ALMA data with the goal of exploring the molecular outflows and their relations with the large-scale orientation of the filaments and magnetic fields. These targets were carefully selected from a large sample of H II regions (Liu et al. 2016a), and hence are comparatively evolved with respect to the IRDC studied by Wang et al. (2011, 2012) and Kong et al. (2019). The molecular line observations of a large sample of H II regions were performed using the Atacama Submillimeter Telescope Experiment 10 m telescope. These particular 11 targets showed a strong blue-emission profile of HCN (4–3), which is an efficient tracer of infalling gas. Hence, these targets are ideal to search for the gas dynamics and the molecular outflows. Additionally, most of these targets are embedded within large-scale filaments, while the remaining are associated with circular clumps. Thus, studying these targets will provide a unique opportunity to examine the influence of large-scale filamentary structures on the protostellar outflows in a slightly evolved massive star-forming region (i.e., H II region) compared to young IRDCs (Wang et al. 2011; Kong et al. 2019), and to compare with the outflows in circular clumps. We followed up these 11 targets using ALMA for a comprehensive study. The parameters of the target regions are detailed in Table 1.

The distances of our target sources were reported in Faúndez et al. (2004). However, we recalculated the distances using a renewed Galactic rotation model. The local standard of rest velocities (v_{lsr}) were obtained from Liu et al. (2016a). These distances were estimated using a python-based “Kinematic Distance Calculation Tool” of Wenger et al. (2018), which evaluates a Monte Carlo kinematic distance adopting the solar Galactocentric distance of 8.31 ± 0.16 kpc (Reid et al. 2014). Corresponding near kinematic distances generally agreed well with the distance estimates reported in Faúndez et al. (2004). The distances listed in Table 1 are near kinematic distance to our targets. In this paper, we only present the CO outflows, and detailed studies of the gas dynamics and chemistry will be presented in subsequent papers. This study is organized as follows. Section 2 describes the observations and the archival data used in the analysis. In Section 3, we present the procedure for identifying the outflows, identification of filaments, estimation of magnetic fields’ position angles (PAs) and analysis of observed outflow parameters. Section 4 presents a discussion of the overall scenario. Finally, we summarize the study in Section 5.

2. Data

2.1. ALMA Observations

Observations of these targets were carried out from 2018 May 18 to 20 (UTC) (ALMA Cycle 5), under the project 2017.1.00545.S (PI: Tie Liu) using 43 12 m antennas in C43-1 configuration. To cover multiple molecular lines, the observations were obtained in four spectral windows in Band 7 (centering at 343.2, 345.1, 354.4, and 356.7 GHz) that are good tracers of infalling and outflowing gas, along with continuum. In this paper, we present CO(3–2) line observations covered in the 345.1 GHz centered spectral band. A baseband of 1.88 GHz with

Table 1
Details of Targets

Source	R.A. (J2000)	Decl. (J2000)	V_{LSR} (km s^{-1})	Distance ^a (kpc)	PA_{Fil} (deg)	θ_B (deg)	PA_{Gal} (deg)
IRAS 14382-6017	14 42 02	−60 30 35	−60.55	4.1 ± 0.6	65	71 ± 4	66
IRAS 14498-5856	14 53 42	−59 08 56	−50.03	3.2 ± 0.5	40	61 ± 10	63
IRAS 15520-5234	15 55 48	−52 43 06	−41.25	2.6 ± 0.4	—	50 ± 6	50
IRAS 15596-5301	16 03 32	−53 09 28	−74.44	4.4 ± 0.5	—	50 ± 12	49
IRAS 16060-5146	16 09 52	−51 54 54	−89.95	5.2 ± 0.6	120	50 ± 5	47
IRAS 16071-5142	16 11 00	−51 50 21	−86.67	4.9 ± 0.7	58	41 ± 3	47
IRAS 16076-5134	16 11 27	−51 41 56	−87.32	5.0 ± 0.7	48	47 ± 13	47
IRAS 16272-4837	16 30 59	−48 43 53	−46.42	3.2 ± 0.3	—	41 ± 10	43
IRAS 16351-4722	16 38 49	−47 28 03	−40.64	2.9 ± 0.4	45	68 ± 32	42
IRAS 17204-3636	17 23 50	−36 38 58	−17.94	2.9 ± 0.6	—	36 ± 7	34
IRAS 17220-3609	17 25 24	−36 12 45	−94.67	7.6 ± 0.3	24	30 ± 32	34

Notes. PA_{Fil} values marked with “—” indicate a target is not associated with filaments.

^a Distances estimated using the Kinematic Distance Calculation Tool of Wenger et al. (2018, <http://www.treywenger.com/kd/>).

a spectral resolution of 1.13 MHz was used for the CO (3–2) observations. In these observations J1427-4206 and J1924-2914 were used as phase and bandpass calibrators, while JJ1524-5903, 1650-5044, and J1733-3722 were observed as phase calibrators during our three-epoch ALMA observations. We performed self-calibration and cleaned the data cube using the `tclean` task in CASA 5.1.1. Briggs weighting with a robust number of 0.5 was used, and resulted in a final synthesized beam size of $0''.8 \times 0''.7$. The average cube sensitivity is $8.3 \text{ mJy beam}^{-1}$ with 1 km s^{-1} wide velocity channels. We also used 0.9 mm ALMA continuum images and catalog values in this paper to identify the driving sources of the observed outflows. The details from the identification of continuum sources and corresponding analyses will be presented in a forthcoming paper.

2.2. Molecular Line Data

In order to identify the large-scale host molecular clouds and filamentary structures of our target regions, we used publicly available ^{13}CO ($J = 1-0$) line maps of the Three-mm Ultimate Mopra Milky Way Survey (ThrUMMS; Barnes et al. 2015). The ThrUMMS survey data has an angular resolution of $66''$ and a velocity resolution of 0.34 km s^{-1} , with an rms noise of 0.7 K km s^{-1} (see Table 2 of Barnes et al. 2015).

2.3. Submillimeter Data

The APEX Telescope Large Area Survey of the Galaxy (ATLASGAL; Schuller et al. 2009) imaged the inner Galactic plane ($|l| \leq 60^\circ$ and $|b| \leq 1.5^\circ$) at $870 \mu\text{m}$ with the Large APEX Bolometer Camera (Siringo et al. 2009). The ATLASGAL survey data has an FWHM resolution of $19''.2$. The ATLASGAL images were also used for our target regions to identify the filamentary structures.

2.4. Dust Polarization Data

Numerical studies show that the orientation of outflows depends on the direction of magnetic fields. Thus, to estimate the magnetic field orientation toward our target fields we obtained the *Planck*,¹⁷ 353 GHz ($850 \mu\text{m}$) dust continuum polarization data (Planck Collaboration et al. 2016a). The data comprising of Stokes I , Q , and U maps were extracted from the

Planck Public Data Release 2 (Planck Collaboration et al. 2016b) of Multiple Frequency Cutout Visualization (PR2 Full Mission Map with PCCS2 Catalog).¹⁸ The maps have a pixel scale of $\sim 1'$ and beam size of $\sim 5'$.

3. Results

3.1. Identification of Outflows

For identification of outflows, we cropped the observed ALMA data cubes for each region into smaller cubes that only cover $\pm 200 \text{ km s}^{-1}$ centering on the systematic velocity of each target. These smaller data cubes were also averaged to a resolution of 5 km s^{-1} (i.e., 5 channels of original data cube) for enhancing the signal-to-noise ratio to trace the outflows more easily. We carefully examined these small data cubes by looking for the red–blue lobes around continuum sources. It is convenient to start with the high-end redshifted and blueshifted velocities in the data cubes, as these channels are least contaminated from emission from the central clouds. In addition to the bipolar outflows, we identified single outflows that are associated with continuum sources, and also a few outflows without any association with continuum sources.

After completing the preliminary identification of outflows in the averaged small data cubes, we inspected the original data cubes for the same set of outflows to obtain their final parameters. This also helped us to identify lower-velocity outflows that were not detected in the integrated channel maps. In addition, other outflow tracers of outflows (e.g., HCN, SiO) were used to confirm a few confusing outflow lobes. The peak velocity and extent of each outflow were considered up to a 5σ level, where σ is the rms measured from a few line-free channels. The details of all identified outflows, such as the coordinates of the continuum sources, assigned names, orientations of outflow lobes in the plane of sky, orientation of lobes with respect to underlying filaments, magnetic field orientation and Galactic plane (see following sections), peak velocity, and extent of each outflow, are presented in Table 2. For five outflow lobes, no continuum sources were detected, as they are possibly below our detection limit. The outflow lobes overlaid on the 0.9 mm ALMA continuum maps for all the regions are presented in Figure 1. We identified a total of 105 outflow lobes. Among them 32 are bipolar and 41 are unipolar in nature.

¹⁷ <http://www.esa.int/Planck>

¹⁸ <https://irsa.ipac.caltech.edu/applications/planck/>

Table 2
Outflow Parameters

Continuum Source		Outflow Name	PA _{lobe} (°)		γ _{Fil} (°)		γ _B (°)		γ _{GP} (°)		v _{peak} (km s ^{−1})		Extent (pc)		
R.A. (J2000)	Decl. (J2000)		Red	Blue	Red	Blue	Red	Blue	Red	Blue	Red	Blue	Red	Blue	
14 42 02.106	−60 30 44.59	I14382_o1a	37	52	−28	−13	−34	−19	−29	−14	49.5	46.7	0.041	0.067	
		I14382_o1b	−38	...	77	...	71	...	76	...	55.6	...	0.148	...	
14 42 03.066	−60 30 26.02	I14382_o2	66	72	1	7	−5	1	0	6	70.4	72.7	0.067	0.070	
14 42 02.833	−60 30 49.99	I14382_o3	−38	...	77	...	71	...	76	...	31.3	...	0.083	...	
14 53 42.681	−59 08 52.88	I14498_o1a	−74	...	73	...	45	...	43	...	119.0	...	0.263	...	
		I14498_o1b	...	71	...	38	...	10	...	8	...	65.6	...	0.190	...
^a	^a	I14498_o2	82	83	49	50	21	22	19	20	65.3	69.1	0.054	0.054	
14 53 43.579	−59 08 43.78	I14498_o3	57	...	24	...	−4	...	−6	...	19.3	...	0.213	...	
14 53 42.941	−59 09 00.87	I14498_o4	6	...	−27	...	−55	...	−57	...	25.4	...	0.151	...	
15 55 48.398	−52 43 06.53	I15520_o1	25	26	−25	−24	−25	−24	28.1	32.6	0.313	0.206	
15 55 48.654	−52 43 08.66	I15520_o2a	−84	46	...	46	...	42.0	...	0.284	...	
		I15520_o2b	...	−20	−70	...	−70	...	32.6	...	0.236	...
15 55 48.393	−52 43 04.38	I15520_o3	...	7	−43	...	−43	...	23.9	...	0.276	...
15 55 48.848	−52 43 01.61	I15520_o4	...	79	29	...	29	...	61.2	...	0.266	...
15 55 49.265	−52 43 03.02	I15520_o5	...	56	6	...	6	...	68.1	...	0.191	...
16 03 31.921	−53 09 22.96	I15596_o1a	−86	−84	44	46	45	47	41.7	48.4	0.480	0.415	
		I15596_o1b	85	89	35	39	36	40	33.1	54.5	0.196	0.248	
16 03 32.646	−53 09 26.82	I15596_o2a	−65	−54	65	76	66	77	88.5	51.0	0.079	0.066	
		I15596_o2b	69	64	19	14	20	15	72.9	84.9	0.045	0.037	
16 03 32.656	−53 09 45.76	I15596_o3	−24	−74	...	−73	...	55.6	...	0.123	...	
16 03 32.705	−53 09 29.57	I15596_o4	15	3	−35	−47	−34	−46	49.5	42.4	0.123	0.203	
16 03 31.697	−53 09 32.09	I15596_o5	−76	−82	54	48	55	49	104.1	95.3	0.160	0.261	
^a	^a	I15596_o6	71	71	21	21	22	22	72.1	51.0	0.148	0.148	
16 03 32.927	−53 09 27.85	I15596_o7	...	−53	77	...	78	...	33.7	...	0.130	...
16 03 30.635	−53 09 33.99	I15596_o8	...	−68	62	...	63	...	82.3	...	0.175	...
16 09 52.650	−51 54 54.86	I16060_o1	−82	−82	−22	−22	48	48	51	51	40.1	34.5	0.488	0.223	
16 09 52.450	−51 54 55.79	I16060_o2	...	73	...	−47	...	23	...	26	...	50.1	...	0.488	...
^a	^a	I16060_o3	50	...	−70	...	0	...	3	...	39.2	...	0.416	...	
16 09 52.803	−51 54 57.90	I16060_o4	−42	...	18	...	88	...	−89	...	26.2	...	0.662	...	
16 10 59.750	−51 50 23.54	I16071_o1a	−83	−89	44	38	56	50	50	44	70.2	56.3	0.571	0.387	
		I16071_o1b	83	86	30	33	42	45	36	39	31.2	35.5	0.264	0.380	
		I16071_o1c	43	54	−10	1	2	13	−4	7	52.9	39.9	0.213	0.158	
		I16071_o1d	...	84	...	31	...	43	...	37	...	142.2	...	0.240	...
		I16071_o1e	...	−75	...	52	...	64	...	58	...	90.1	...	0.465	...
16 10 59.553	−51 50 27.51	I16071_o2	−7	−23	−60	−76	−48	−64	−54	−70	148.3	109.2	0.054	0.045	
16 10 59.400	−51 50 16.52	I16071_o3	78	81	25	28	37	40	31	34	31.2	28.6	0.371	0.154	
16 11 00.242	−51 50 26.22	I16071_o4	...	−42	...	85	...	−83	...	−89	...	19.1	...	0.299	...
16 10 58.732	−51 50 36.37	I16071_o5	62	...	9	...	21	...	15	...	31.2	...	0.183	...	
16 10 59.286	−51 50 11.78	I16071_o6	71	67	18	14	30	26	24	20	33.8	94.5	0.054	0.047	
16 10 59.286	−51 50 11.78	I16071_o7	−1	6	−54	−47	−42	−35	−48	−41	87.6	65.9	0.145	0.142	
16 11 26.540	−51 41 57.32	I16076_o1a	51	47	14	10	4	0	4	0	85.2	41.4	0.136	0.080	
		I16076_o1b	18	20	−19	−17	−29	−27	−29	−27	111.2	27.5	0.144	0.120	
		I16076_o1c	−59	...	84	...	74	...	74	...	68.7	...	0.162	...	
		I16076_o1d	76	64	39	27	29	17	29	17	80.9	87.3	0.066	0.107	
		I16076_o1e	−62	...	81	...	71	...	71	...	35.8	...	0.184	...	
		I16076_o1f	−45	...	−82	...	88	...	88	...	35.8	...	0.216	...	
		I16076_o1g	71	72	34	35	24	25	24	25	35.8	63.1	0.205	0.098	
		I16076_o1h	−50	−71	−87	72	83	62	83	62	32.3	31.0	0.170	0.203	
		I16076_o1i	...	6	...	−31	...	−41	...	−41	...	56.1	...	0.194	...
		I16076_o1j	...	30	...	−7	...	−17	...	−17	...	32.7	...	0.166	...
		I16076_o1k	...	−35	...	−72	...	−82	...	−82	...	52.7	...	0.108	...
		I16076_o1l	...	−37	...	−74	...	−84	...	−84	...	35.3	...	0.128	...
16 11 27.384	−51 41 50.21	I16076_o2	−12	...	−49	...	−59	...	−59	...	35.8	...	0.412	...	
16 11 27.697	−51 41 55.36	I16076_o3	...	−36	...	−73	...	−83	...	−83	...	36.2	...	0.299	...
16 11 26.876	−51 41 55.92	I16076_o4	−89	...	54	...	44	...	44	...	36.6	...	0.155	...	
16 11 26.876	−51 41 55.92	I16076_o5	...	−88	...	55	...	45	...	45	...	37.9	...	0.076	...
^a	^a	I16076_o6	...	84	...	47	...	37	...	37	...	23.2	...	0.167	...
16 30 58.770	−48 43 53.89	I16272_o1a	25	29	−16	−12	−18	−14	68.0	41.2	0.256	0.209	
		I16272_o1b	−31	−28	−72	−69	−74	−71	22.9	20.4	0.254	0.359	
		I16272_o1c	87	46	...	44	...	31.6	...	0.122	...	
^a	^a	I16272_o2	74	33	...	31	...	47.2	...	0.184	...	
16 38 50.501	−47 28 00.91	I16351_o1a	58	41	19	2	−10	−27	16	−1	92.0	21.6	0.090	0.092	
		I16351_o1b	...	46	...	7	...	−22	...	4	...	35.4	...	0.237	...
17 23 50.249	−36 38 59.66	I17204_o1a	81	82	45	46	47	48	20.2	40.5	0.144	0.123	
		I17204_o1b	...	−77	67	...	69	...	32.7	...	0.179	...
		I17204_o1c	...	−67	77	...	79	...	35.3	...	0.175	...
		I17204_o1d	...	2	−34	...	−32	...	24.9	...	0.342	...
17 25 25.635	−36 12 35.12	I17220_o1	68	71	68	71	38	41	34	37	28.4	32.3	0.196	0.215	
17 25 24.796	−36 12 36.85	I17220_o2	−65	−48	−65	−48	85	−78	81	−82	97.8	49.6	0.265	0.280	
17 25 24.357	−36 12 47.89	I17220_o3	13	17	13	17	−17	−13	−21	−17	35.4	55.7	0.316	0.264	

Table 2
(Continued)

Continuum Source		Outflow Name	PA _{lobe} (°)		γ_{Fil} (°)		γ_B (°)		γ_{GP} (°)		v_{peak} (km s ⁻¹)		Extent (pc)	
R.A. (J2000)	Decl. (J2000)		Red	Blue	Red	Blue	Red	Blue	Red	Blue	Red	Blue	Red	Blue
17 25 24.453	-36 12 39.36	I17220_o4	13	10	13	10	-17	-20	-21	-24	33.6	52.2	0.140	0.238
17 25 24.926	-36 12 43.44	I17220_o5	41	...	41	...	11	...	7	...	30.2	...	0.076	...
17 25 25.697	-36 12 39.48	I17220_o6	62	...	62	...	32	...	28	...	34.5	...	0.080	...

Note.

^a No continuum sources are detected for these outflows.

3.2. Identification of Host Clouds and Filaments

The primary aim of our study is to examine whether the orientation of outflow lobes has a dependence on large-scale filamentary accretion and also with the orientation of the magnetic fields or Galactic plane. Thus, we examined integrated ThrUMMS ¹³CO maps and the ATLASGAL dust continuum maps to identify the host clouds and large-scale filamentary structures. To generate the integrated intensity maps, the velocity ranges of all the clouds were determined from the ¹³CO spectrum along the direction of each target. Priority is given to the cloud structures traced in ThrUMMS ¹³CO data over the ATLASGAL images, as the integrated ¹³CO data for a specific velocity range suffers from the least contamination from the foreground and background emission compared to ATLASGAL maps. However, ¹³CO data were not available for IRAS 17204-3636 and IRAS 17220-3609 regions. Thus, for these two regions, we identified clouds based on the 870 μ m ATLASGAL image.

The Python-based FILFINDER algorithm (Koch & Rosolowsky 2015) was applied on all the identified molecular clouds to trace the filamentary structures. FILFINDER is capable of finding filaments even with low surface brightness, as the algorithm uses an arctangent transform on the image. This algorithm identifies all the possible filamentary structures across the input map followed by a method to determine their skeletons via the Medial Axis Transform. To identify the filaments, we ran the FILFINDER algorithm with inputs like the global background thresholds and thresholds for length of skeletons. Note that the primary beam of our ALMA data (36'') is comparable or even smaller than the angular resolution of the ATLASGAL (19'') and ThrUMMS ¹³CO data (66'') making it difficult to determine the filament orientation at the scale of ALMA field of view (PA_{Fil}). So, we only considered the large-scale PAs of filaments estimated by a visual fit over the large-scale FILFINDER skeletons. By large-scale PAs, we mean the average PAs over at least 5 pixels of the identified skeleton (i.e., ~ 3 –4 pc at the distances of our targets). Note that a visual fit to filaments might not be as accurate as a statistical fit. However, visual fits to these large-scale PA_{Fil} have typical uncertainty $\lesssim 10^\circ$. We also considered elongated clumps (aspect ratio < 5) as filamentary structure because such structures may also aid the gas flow along a preferred direction, like filaments.

Filaments are detected toward seven targets, and corresponding PA_{Fil} are listed in Table 1. The remaining four targets are associated with round clumps that have no preferred orientations. The distribution of integrated ¹³CO and dust emission toward two representative regions, one with filaments (IRAS 16351-4722) and another without filaments (IRAS 15520-5234), are shown in Figures 2 and 3. The extents of the

identified clouds are also marked in both figures. We have also shown the *Planck* 850 μ m dust emission, as *Planck* data are used to determine the magnetic field PAs in our study (see the following section). The filament mask identified by the FILFINDER algorithm, and a visual fit to the filament, are also shown in Figure 2(d). Figures corresponding to the remaining targets are presented in Appendix A.

3.3. Magnetic Field Position Angle

We use *Planck* polarization data to infer the mean orientation of the magnetic field around our targets, as magnetic fields often aid in star formation. We estimated the mean linear polarization PAs over the cloud extent identified in the previous section. The conventional relation for PAs, $\theta_{\text{GAL}} = 0.5 \times \arctan(U, Q)$ (where, \arctan avoids the π ambiguity) yields PAs in Galactic coordinates in the range $-90^\circ < \theta < +90^\circ$, where $\theta_{\text{GAL}} = 0^\circ$ pointing toward the Galactic North but increasing toward Galactic West. But in order to follow the IAU convention (i.e., $\theta_{\text{GAL}} = 0^\circ$ points Galactic North but increases toward Galactic East), the θ_{GAL} values were derived using the relation

$$\theta_{\text{GAL}} = 0.5 \times \arctan(-U, Q). \quad (1)$$

The magnetic field orientations in Galactic coordinates can be obtained by adding 90° to θ_{GAL} , i.e., $\theta'_B = 90^\circ + \theta_{\text{GAL}}$ (for details see Planck Collaboration et al. 2016c, 2016d, and references therein).

Furthermore, the magnetic field orientation in celestial coordinates (FK5, J2000) is obtained using the following relation given in Corradi et al. (1998):

$$\psi = \arctan \left[\frac{\cos(l - 32^\circ 9')}{\cos b \cot 62^\circ 9' - \sin b \sin(l - 32^\circ 9')} \right], \quad (2)$$

where ψ is the angle subtended at the position of each object by the direction of the equatorial North and the Galactic North. l and b are the Galactic coordinates of each pixel with a polarization measurement. We then transform the magnetic field orientations from a Galactic (θ'_B) to an equatorial (θ_B) coordinate system using the relation

$$\theta_B = \theta'_B - \psi. \quad (3)$$

Finally, we have estimated the mean magnetic field orientation using the θ_B vectors distributed within the area of the clouds identified in the previous section. The mean values of θ_B and the corresponding standard deviations are listed in Table 1. The mean magnetic field directions toward IRAS 14498-5856 and IRAS 15520-5234 regions are also marked in Figures 2(d) and 3(d).

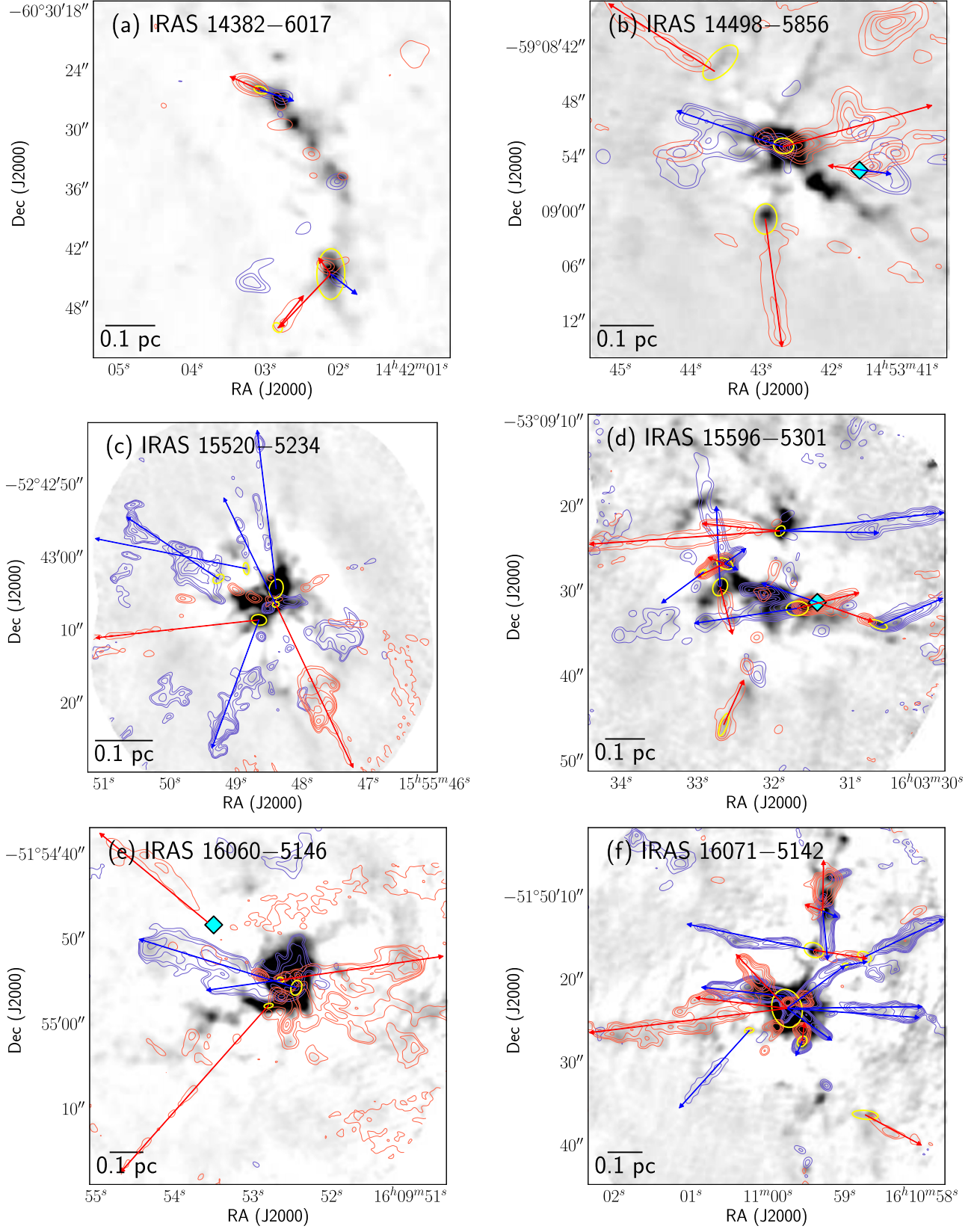


Figure 1. Images of molecular outflows in the first six target fields listed in Table 1. The background grayscale images are the ALMA 0.9 mm continuum maps. The red and blue contours correspond to redshifted and blueshifted CO(3–2) gas integrated over carefully selected velocity ranges to depict the outflow lobes. The blue and red outflow lobes are also marked by blue and red arrows, respectively. The driving sources as shown by continuum emission are marked with yellow ellipses. The outflow lobes marked with cyan diamonds have no continuum sources identified.

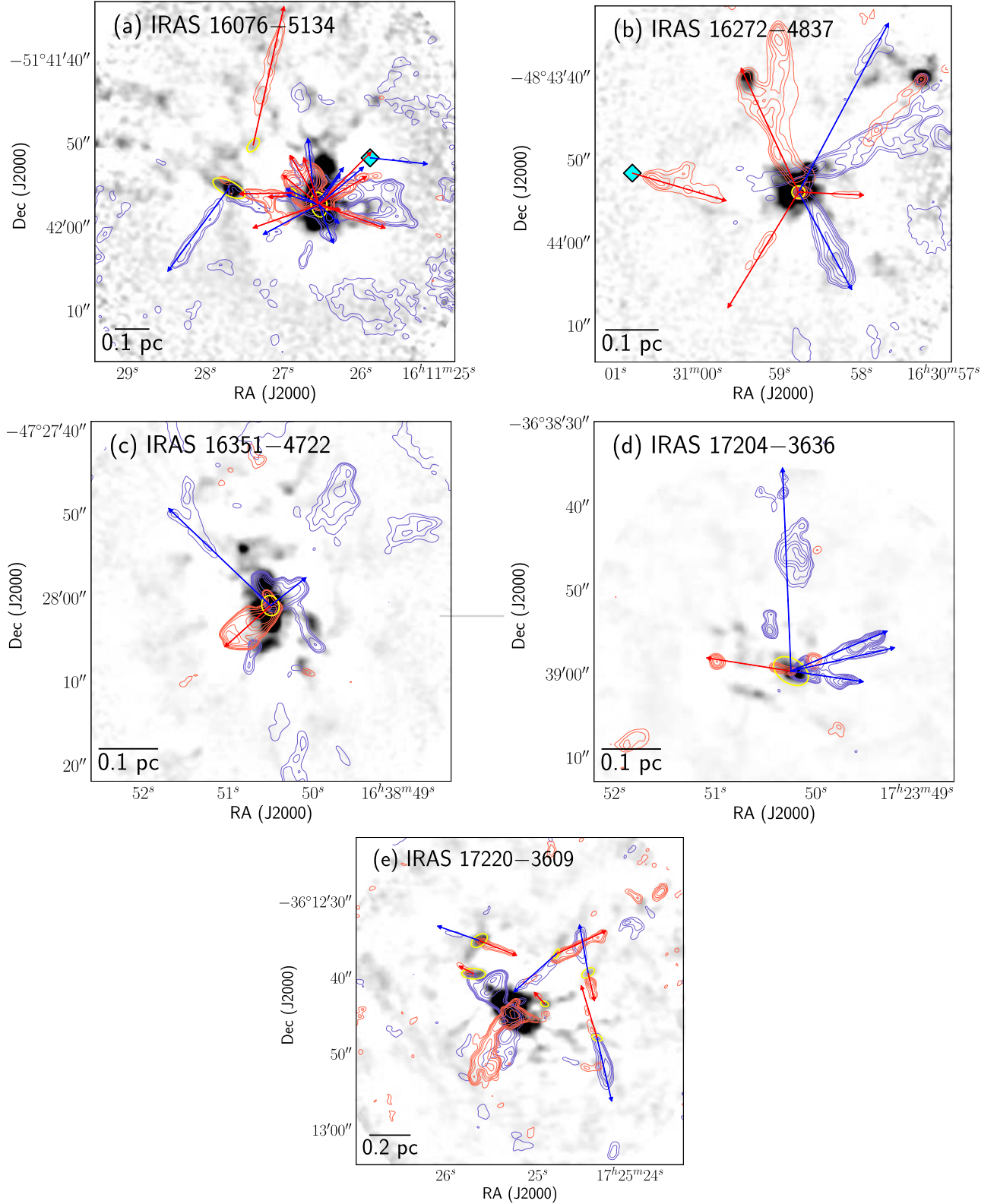


Figure 1. (Continued.)

3.4. Statistics of Outflow Extent and Velocities

We have measured the projected plane-of-sky extent and maximum red-blue velocities of all identified outflow lobes. The plane-of-sky extents of outflow lobes are converted into physical

scale (in parsecs) using the distances listed in Table 1. A histogram for all the measured outflow extents is presented in Figure 4(a), along with the histograms for extents of red and blue lobes separately. Red and blue lobes typically show a similar shape signifying an unbiased identification of the outflow lobes.

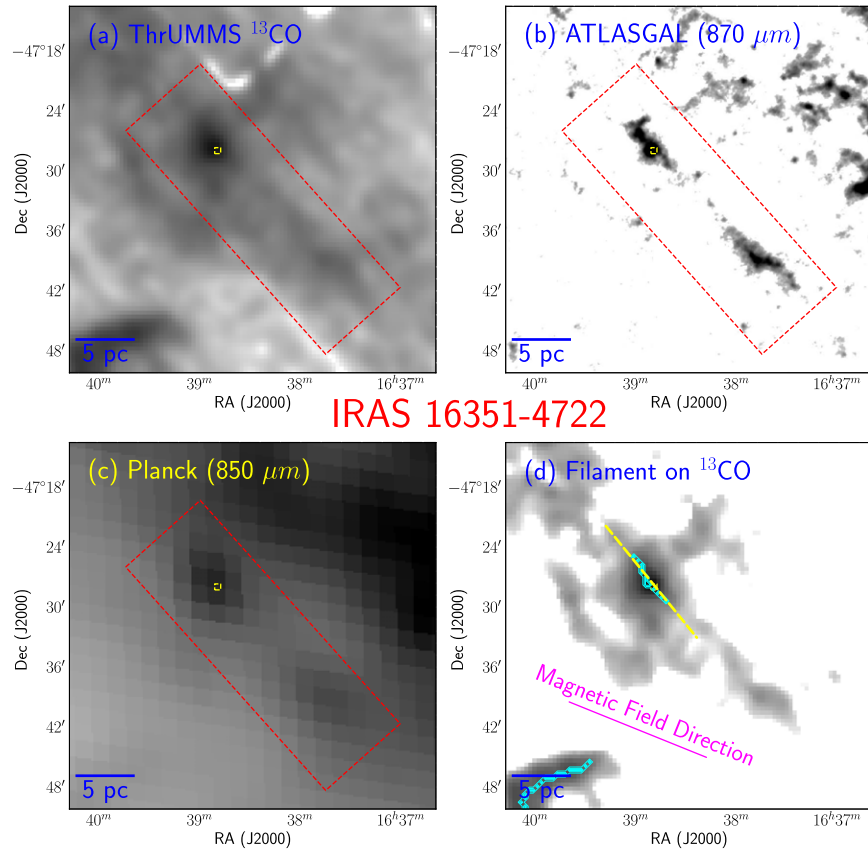


Figure 2. Distribution of gas and dust in the IRAS 16351-4722 region. (a) Velocity-integrated ThrUMMS ^{13}CO map of the large $21' \times 21'$ area around IRAS 16351-4722. The field of view of ALMA observations is shown by a small yellow box toward the center. The red rectangle shows the extent of the cloud. (b) ATLASGAL $870\ \mu\text{m}$ dust image of the same area. (c) *Planck* $850\ \mu\text{m}$ image of the same area. (d) Filaments marked on the ThrUMMS ^{13}CO map. The filament skeletons are also shown by cyan contours. The large-scale orientation of the filament is shown by an eye-fitted yellow dashed line. The position angle of the magnetic field is shown by a magenta line. The magnetic field PA is estimated by averaging the polarization position angles of the *Planck* $850\ \mu\text{m}$ dust polarization map within the dashed red rectangle shown in other panels.

Sky-projected extents of outflows lobes have a range of $0.05\text{--}0.7$ pc, peaking at around 0.2 pc. Similarly, we constructed a histogram for peak outflow velocities, which is presented in Figure 4(b). Most outflows have plane-of-sky projected velocities below $50\ \text{km s}^{-1}$. However, a few outflows are seen with significantly higher velocities (up to $150\ \text{km s}^{-1}$), and a few have extended outflow lobes larger than 0.2 pc. With an average outflow extent of 0.2 pc and peak outflow velocity of $40\ \text{km s}^{-1}$, the typical dynamical timescale is about 5×10^3 yr. The average mass of the driving continuum sources is $15 M_{\odot}$ (with $T_{\text{dust}} \sim 20\ \text{K}$ and spectral index, $\beta \sim 2.0$) and the typical outflowing mass is $0.5 M_{\odot}$ (details are not presented in this paper). Such extended massive outflow lobes can be the result of energetic driving protostars. Understanding this scenario requires a detailed analysis of gas dynamics and the momentum budgets of the outflows, which will be presented in a forthcoming paper.

3.5. Outflow Position Angles

The PAs of all outflow lobes (PA_{lobe}) were measured from the celestial North pole. The PAs for both blueshifted and redshifted lobes are measured independently. We are only interested in the orientations of the lobes, hence we have allotted them values in the range from -90° to $+90^\circ$ counterclockwise from the celestial North (see Table 2). Thus, the PAs in the first quadrant have negative signs, and those in the second quadrant have positive signs.

We constructed histograms of the absolute values of the measured PA_{lobe} (ignoring the signs), considering each lobe independent (Figure 5). Histograms are constructed separately for the outflows associated with the filaments and with round/circular clumps. The outflows associated with circular clumps can be treated as a control region, as they do not have any preferred direction of gas accretion like filaments. Although the overall distribution of PA_{lobe} has a rising trend at $\sim 90^\circ$, lobes associated with filaments do not have any preferred plane-of-sky direction (Figure 5(a)). The distribution is skewed toward $\text{PA}_{\text{lobe}} = 90^\circ$, as the outflow lobes associated with the circular clumps are mostly oriented at PA_{lobe} in the range from 50° to 90° .

3.5.1. PA_{lobe} with Respect to Magnetic Field and Galactic Plane

As mentioned before, magnetic fields play important roles at different evolutionary phases and spatial scales of star formation. Hence, in this study we also searched for any correlation of the PA_{lobe} with respect to the large-scale magnetic field orientation. We measured the projected plane-of-sky angles between PAs of large-scale magnetic field (see θ_B values in Table 1) and PA_{lobe} (hereafter γ_B). The following equation was used to estimate the γ_B values:

$$\gamma_B = \text{MIN}\{|\text{PA}_{\text{lobe}} - \theta_B|, |\text{PA}_{\text{lobe}} - \theta_B| - 90^\circ\}, \quad (4)$$

where γ_B has ranges between 0° and 90° .

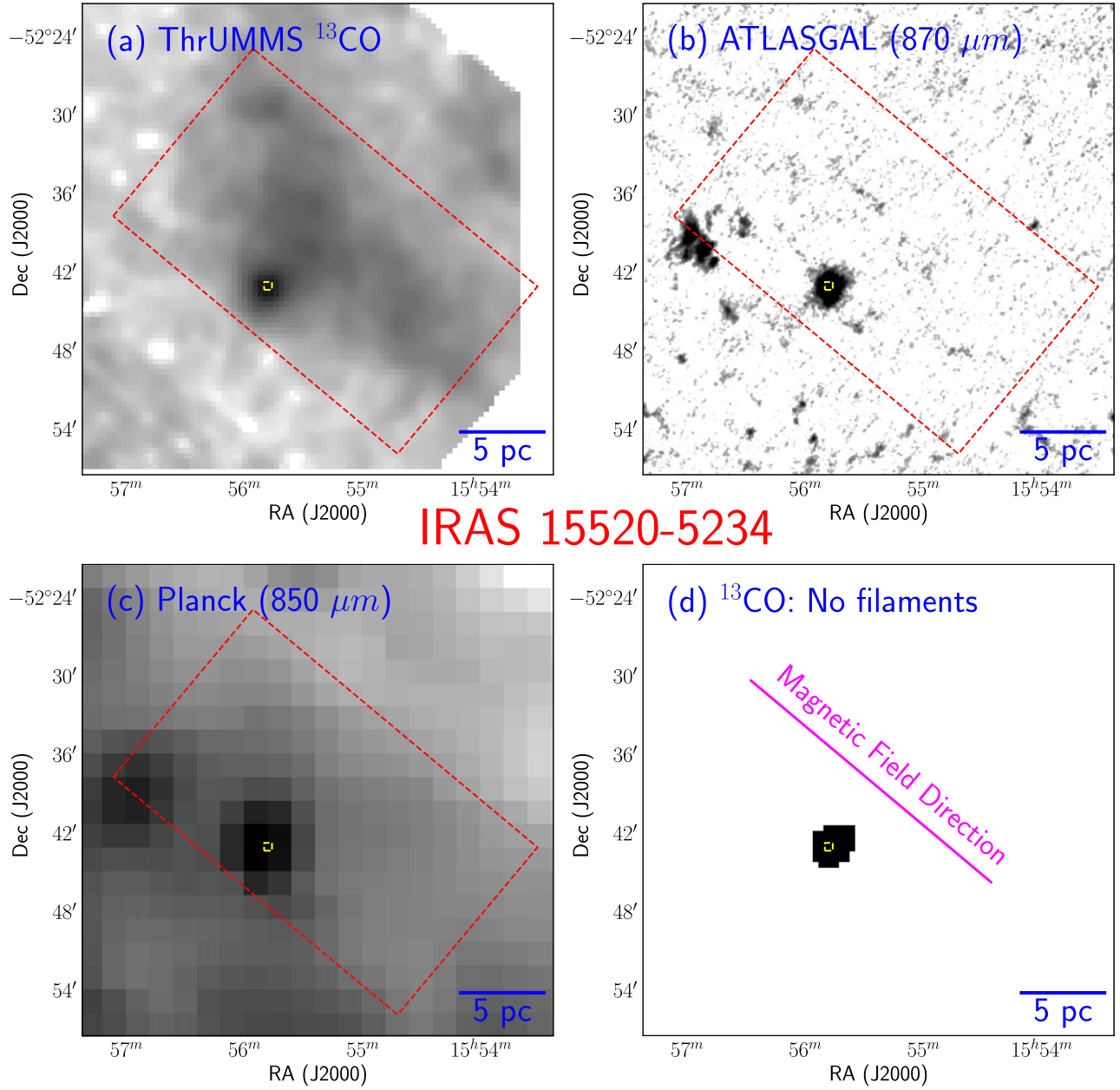


Figure 3. Distribution of gas and dust in the IRAS 15520-5234 region where no filamentary structure is detected in the integrated ^{13}CO and ATLASGAL 870 μm images. The symbols are the same as those in Figure 2.

Note that previous studies of Galactic large-scale filaments showed most of them generally aligned with the Galactic plane (Wang et al. 2015, 2016). Thus, it might be important to also examine the projected plane-of-sky angles between PAs of Galactic plane (i.e., PA_{GP} ; see Table 1) and PA_{lobe} (hereafter γ_{GP}). The γ_{GP} values are calculated with a convention similar to that in Equation (4).

Histograms for both γ_B and γ_{GP} are shown in Figure 5(b). No specific trend in the distributions is noted in both cases. This particular result suggests a noncorrelation of the outflow axes with the large-scale magnetic field orientation as well as the Galactic plane.

3.5.2. Orientation of Outflows and Filaments

Our primary interest in this paper is to search for the presence of any preferred angle of outflows with respect to their host

filaments. Filamentary structures are seen in seven regions (see Section 3.2). These 7 targets contain a total of 49 outflow lobes. The PA_{Fil} values of the identified filaments are listed in Table 1.

We further measured the projected PAs between PA_{lobe} and PA_{Fil} (i.e., γ_{Fil}) for all the lobes in these seven regions following the same convention used in Equation (4). In Figure 6(a), we present the histogram of all the γ_{Fil} . In addition, we also provide a histogram of γ_{Fil} for lobes for which the host filaments are oriented along the magnetic field (namely, IRAS 14382-6017, IRAS 14498-5856, IRAS 16071-5142, and IRAS 16076-5134). No specific trend is apparent in the histograms, except both the histograms are slightly devoid of outflow lobes at $\gamma_{\text{Fil}} \sim 60^\circ$. We further constructed a cumulative histogram of γ_{Fil} (Figure 6(b)). It is apparent in the cumulative histogram that γ_{Fil} for all seven regions with filaments, and also filaments aligned with magnetic fields, do not show any specific trend. In

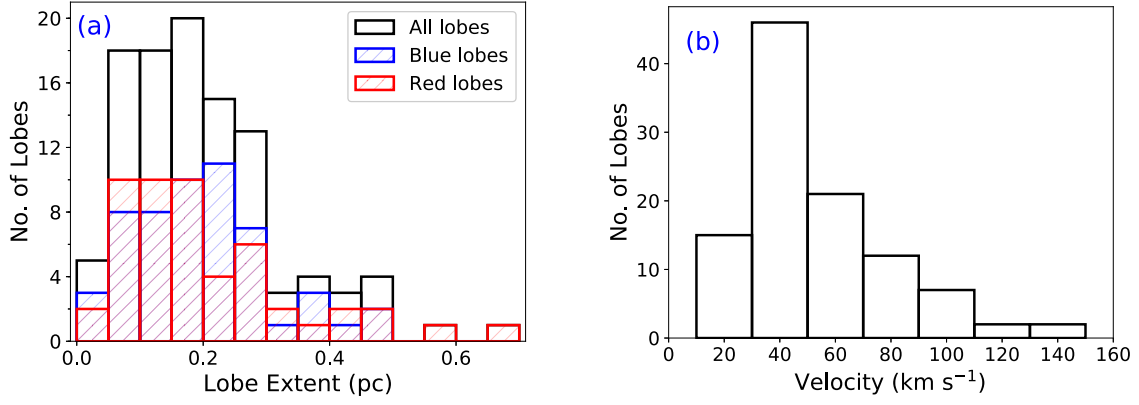


Figure 4. (a) Stacked histogram of the extents of all the identified outflows. The extents for the blue and red lobes are shown as blue and red histograms. (b) Histogram of the peak velocities of all the identified outflows.

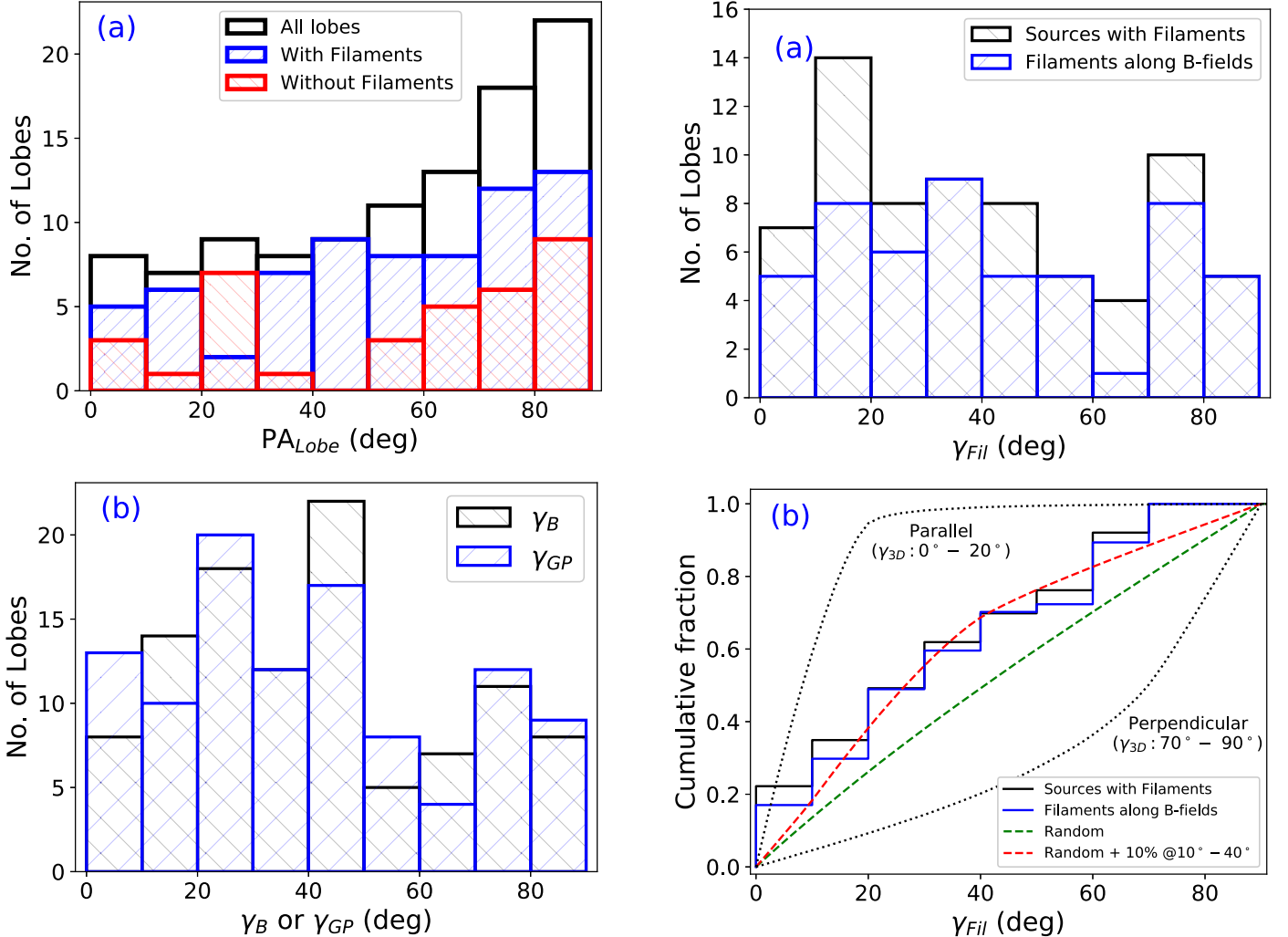


Figure 5. (a) Stacked histogram of the PAs of all the identified outflow lobes associated with filaments and circular clumps. (b) Stacked histograms of the projected separations of the PAs of all the lobes with respect to magnetic field orientation (γ_B) and Galactic plane (γ_{GP}).

fact, the distribution seems to be random in nature, and follows closely the random distribution curve shown in Figure 6(b).

Note that we measured PAs of outflow lobes and filaments on the plane of sky. The measured γ_{Fil} value is thus a plane-of-sky projection of the actual three-dimensional angle between outflow

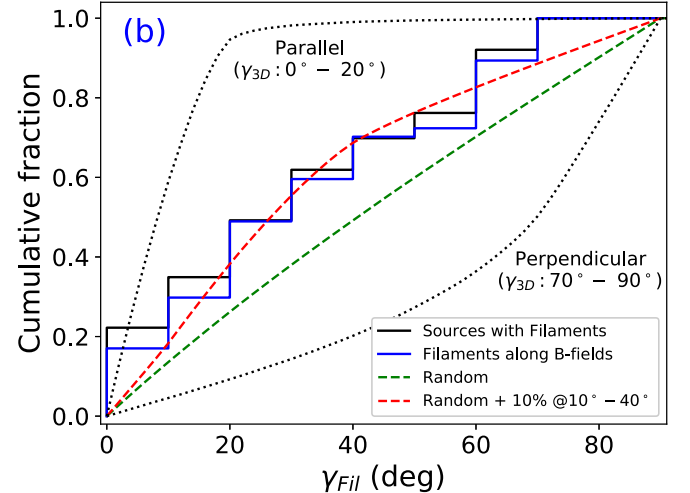


Figure 6. (a) Histogram of γ_{Fil} (i.e., the angle between the PA_{Out} and PA_{Fil}). (b) Cumulative distribution function of γ_{Fil} . The green line shows the CDF of randomly distributed γ_{3D} values. The two black dotted lines show parallel and perpendicular distributions of γ_{3D} values. The red line represent the CDF for the randomly distributed γ_{3D} values, with an additional 10% of sources that are oriented along 10°–40°. The red line better represents the observed CDF of γ_{Fil} .

axes and their host filaments (γ_{3D}). Hence, the observed γ_{Fil} values might appear with a different distribution than the original distribution of γ_{3D} (see detailed discussions by Stephens et al. 2017). To examine the projection effects on the measured γ_{Fil}

distribution, we carried out a Monte Carlo simulation. The detailed methodology can be found in Stephens et al. (2017). In brief, we randomly generated 2×10^6 radially outward pairs of unit vectors on the surface of a sphere. Then we calculated the real 3D PA between the two unit vectors (γ_{3D}), and also their 2D PA (γ_{2D}), assuming they are projected onto the y - z plane. These γ_{2D} values are equivalent to the observed γ_{Fil} . Finally, we calculated the cumulative distribution function (CDF) of γ_{2D} , considering three scenarios of γ_{3D} values: (1) parallel, with γ_{3D} ranging from 0° to 20° ; (2) perpendicular, with γ_{3D} ranging from 70° to 90° ; and (3) random, with γ_{3D} ranging from 0° to 90° . These simulated CDFs are also shown in Figure 6(b). Although, our observed CDF of γ_{Fil} typically follows the random distribution, it also deviates slightly. We thus tried a combined CDF for random and γ_{3D} values from 10° to 40° that may better represent the observed CDF of γ_{Fil} . Accordingly, we found that the observed distribution γ_{Fil} can be reproduced if an additional 10% of sources in a random distribution have preferred γ_{3D} values from 10° to 40° . Note that the uncertainties in the measured PAs are about $\sim 10^\circ$. Thus, the simulated CDF with 10% more sources in a preferred direction from 10° to 40° , which better represents the observed γ_{Fil} CDF, might not be significant.

4. Discussion

The projected momentum axes of outflow lobes in our studied protoclusters do not show any preferred direction with respect to the observed filaments. The γ_{Fil} are in fact distributed in a random fashion (see Figure 6(b)). For further confirmation of the randomness, we performed a statistical Kolmogorov–Smirnov test on the observed CDF of γ_{Fil} with the simulated CDFs for random and random+preferred (10% in 10° – 40°) γ_{3D} values. Both the tests produce p -values greater than 0.8, which imply that we cannot reject the null hypothesis at a level of 80% or lower. This particular test indicates that the distribution is likely to be random in nature (with at least 80% confidence). In addition, our identified outflow lobes do not show any preferred orientation with respect to the large-scale magnetic field, as well as with the Galactic plane.

The random orientation of outflow lobes on the plane of sky for every origin indicates that the distribution of γ_{Fil} is really random in nature. Note that we identified filaments with a visual fit to the FILFINDER skeletons, and the uncertainties in the large-scale PA_{Fil} are typically $\lesssim 10^\circ$. Thus, we also constructed a cumulative distribution of γ_{Fil} values by adding a random number in the range of $\pm 10^\circ$. The cumulative distribution does not show any significant change compared to the original curve. Two such examples are shown in Figure 9 in Appendix B. Thus, a robust identification of filaments may only slightly improve the statistics but not the overall finding of this study.

Filamentary structures in molecular clouds may develop through several physical processes, and accretion through filaments also varies depending on the presence of the magnetic fields (see Stephens et al. 2017, for more detailed discussion). Observational studies of Hacar et al. (2013) and Pineda et al. (2011) suggest that filaments may fragment into smaller substructures, which may significantly affect the initial conditions for protostellar accretion and collapse. These prolate substructures are generally aligned along the filaments (Pineda et al. 2011; Hacar et al. 2013), but this is not always the case (Pineda et al. 2015). Formation of protostars within these arbitrarily distributed smaller substructures may thus lead to a random direction of outflows.

Magnetic fields are known to play a crucial role in both low-mass and high-mass star formation (Hull & Zhang 2019) but only at tens of parsec to sub-parsec scales (Li et al. 2013; Zhang et al. 2014; Santos et al. 2016). The role of the magnetic field becomes less important compared to gravity and angular momentum at the core to disk scale (0.01 pc; Zhang et al. 2014). In a study of low-mass star-forming cores, Hull et al. (2014) found no correlation between outflow axis and envelope magnetic fields. The simulation of Li et al. (2015) showed that the local small-scale (i.e., clump/core scale) magnetic field and filament orientations can be substantially different from the large-scale orientations. The deviation in orientation also depends on the gas density of the cores and filaments. Even if the local magnetic field aligned with the large-scale magnetic field, the turbulence within cores may lead to misalignment of outflow axes and magnetic field (Gray et al. 2018). With *Planck* polarization data, we could only estimate the large-scale (a few parsec) magnetic field, which was compared with the sub-parsec-scale driving sources. The internal dynamics and magnetic field at core-scale could be highly different from that measured on large scales. This could be a possible reason for noncorrelation of θ_B with PA_{lobe} .

Earlier, Davis et al. (2009) and Stephens et al. (2017) found a random alignment of molecular outflows (i.e., momentum axes) with respect to the filament/core directions in nearby Galactic star-forming regions. In contrast, Anathpindika & Whitworth (2008), Wang et al. (2011), and Kong et al. (2019) found that the momentum axes of outflows are preferentially oriented perpendicular to the filaments. Numerical simulations suggest both scenarios are possible depending upon the initial condition of the host cloud that formed the filaments, on their surrounding environment, and the presence of magnetic fields. In fact, momentum axes of outflows may vary significantly depending on how exactly the accretion occurs to the central protostars. For example, Clarke et al. (2017) showed that accretion onto a filament occurring from a turbulent environment may produce vorticity that has angular momentum parallel to the axis of the filament.

However, magnetic fields also play a crucial role in star formation (Machida et al. 2005; Machida et al. 2020; Hull & Zhang 2019). Simulations show that the orientations of outflows with respect to their parent cores (thus, the filaments) could depend strongly on the relative strengths of the magnetic field, turbulence, and rotation (Machida et al. 2005; Offner et al. 2016; Lee et al. 2017). It is important to note that although the feedback from star formation is energetically important (Arce et al. 2011) and is capable of sustaining turbulence even in a low-mass star-forming region (Li et al. 2015), the dynamic flow seems to decouple from the filament in the protostellar accretion phase based on the results here. Li & Klein (2019) suggested for a possibility of perpendicular alignment of momentum axis in the moderately strong magnetized filaments. While some observations revealed magnetic field lines to be perpendicular to the orientation of the filament (see, e.g., Matthews & Wilson 2000; Santos et al. 2016), Galametz et al. (2018) showed a bimodal distribution of outflows with respect to envelope-scale magnetic fields in a few protostars. Earlier, Wang et al. (2012) observed a filament perpendicular to and corresponding with outflow lobes parallel to the magnetic fields.

Most previous studies are based on the nearby star-forming clouds. Observational evidence for both preferred and random orientations of outflow lobes are found in the studied regions. The only distant massive star-forming region with a comprehensive

outflow orientation study is IRDC G28.34+0.06 (Wang et al. 2011, 2012; Kong et al. 2019), and outflows in this region orient perpendicular to the underlying filaments. However, our study with 11 massive protocluster shows a contrasting result. Note that the regions presented in this paper have already appeared with H II regions that are characteristics of newborn massive stars. These regions are at a later evolutionary stage compared to the infrared dark clouds (e.g., those studied by Wang et al. 2011; Kong et al. 2019). With the evolutionary sequence, the outflow power declines and the primary winds tend to dominate over the outflows with the evolution of prestellar cores (Bally 2016). In addition, multiplicity is also a common phenomena in the dense massive star-forming environment. Interaction with companions may significantly affect the protostar's spin (Offner et al. 2016; Lee et al. 2017), and hence may lead to randomly oriented outflow lobes.

Another possibility of random distribution of outflow lobes could be the operating of multiple mechanisms in the same molecular cloud. This is because while some simulations suggest a momentum axis parallel to the filament axis under certain conditions, others suggest a perpendicular momentum axis depending upon a different physical condition of the surrounding environment. Thus, under combined environment and physical conditions, one may ideally expect to see a random orientation of the outflow axes with respect to the filament axis. Stephens et al. (2017) tried to disentangle the observed outflows assuming that they are not purely random in nature, and found a hint of momentum axes tending to align perpendicular to the filament axis. Although not very significant, our analysis shows that $\gamma_{\text{Fil}} \sim 60^\circ$ is devoid of outflows, including the filaments that are aligned along the magnetic fields (see Figure 6). This could also be an indication for the presence of the mechanisms that lead to both parallel and perpendicular outflows.

5. Conclusions

In this comprehensive study, we have investigated the protostellar outflows in 11 massive protoclusters using CO(3–2) line data observed with ALMA. The main results of this study are as follows.

1. We identified a total of 105 outflow lobes in these 11 protoclusters, among which 64 lobes are bipolar, and the remaining 41 are unipolar in nature. Except for five outflow lobes, the remaining outflow lobes are identified with ALMA 0.9 mm continuum cores (detailed results of cores are not presented in this paper).
2. Statistically the identified outflow lobes have a wide range of velocity ($10\text{--}150\text{ km s}^{-1}$) and plane-of-sky extents ($0.1\text{--}0.8\text{ pc}$) with most having velocities below 50 km s^{-1} and average projected plane-of-sky extents of $\sim 0.2\text{ pc}$.
3. Seven out of our 11 targets are embedded in filaments. Analysis of plane-of-sky orientations of PA_{lobe} with respect to the filaments (i.e., γ_{Fil}) hosting their driving sources shows no preferred direction.
4. We have taken into account the plane-of-sky projection effect on the observed γ_{Fil} distribution. The theoretical cumulative distribution function was constructed using the projected two-dimensional angles of vectors on three dimensions generated utilizing Monte Carlo simulations. The cumulative distribution function of the observed γ_{Fil} resembles a random orientation of outflow lobes with respect to the filaments.

5. No correlation is also found for the PA_{lobe} values with respect to the large-scale magnetic fields or Galactic plane position angles. In fact, outflows in filaments aligned along magnetic field PAs also do not show any preferred orientation. Magnetic fields are reported to be less important at the core-scale dynamics of star formation, and our results are consistent with a relatively minor role of the magnetic fields.
6. Our result is inconsistent with the observational study of Wang et al. (2011, 2012) and Kong et al. (2019) for massive star-forming regions. They showed perpendicularly aligned outflows with respect to the filaments. However, our targets are associated with H II regions, and hence are at a later evolutionary stage compared to the IRDC studied by Wang et al. (2011, 2012) and Kong et al. (2019). Thus, the outflow axes might depend on the age of a star-forming protocluster.

Overall, it might be important to explore several other massive protoclusters to get a statistically significant scenario. It is also equally important to explore whether the detailed inner structures of the host filaments, e.g., magnetic field, turbulence, etc., have a role in explaining such contrasting scenarios.

T.B. and K.W. were supported by the National Key Research and Development Program of China through grants 2017YFA0402702 and 2019YFA0405100. T.B. acknowledges funding from the National Natural Science Foundation of China (NSFC) through grant 11633005 and support from the China Postdoctoral Science Foundation through grant 2018M631241. T.B. also likes to thank the PKU-Tokyo Partner fund. K.W. acknowledges additional support by the National Science Foundation of China (11973013, 11721303), and the starting grant at the Kavli Institute for Astronomy and Astrophysics, Peking University (7101502016). We also acknowledge research support from the NSFC through grants U1631102 and 11373010. This work was carried out in part at the Jet Propulsion Laboratory, operated for NASA by the California Institute of Technology. D.L. and C.E. acknowledge support funding from the CAS International Partnership Program No. 114A11KYSB20160008, and the National Natural Science Foundation of China No. 11725313. C.E. also acknowledges funding from grant No. 11988101. This research made use of Astropy, a community-developed core Python package for astronomy (Astropy Collaboration 2018). L.B. acknowledges support from CONICYT grant Basal AFB-170002. L.V.T. thanks the French Ministry of Foreign Affairs (French Embassy in Budapest) and the Hungarian National Office for Research and Innovation (NKFIH) for financial support (Balaton program 40470VL/2017-2.2.5-TÉT-FR-2017-00027). This paper makes use of the following ALMA data: ADS/JAO.ALMA#2017.1.00545.S. ALMA is a partnership of ESO (representing its member states), NSF (USA) and NINS (Japan), together with NRC (Canada), MOST and ASIAA (Taiwan), and KASI (Republic of Korea), in cooperation with the Republic of Chile. The Joint ALMA Observatory is operated by ESO, AUI/NRAO, and NAOJ.

Appendix A Cloud and Filament Identifications

As presented in Section 3.2, we identified the host clouds in the integrated ThrUMMS ^{13}CO maps and the ATLASGAL dust

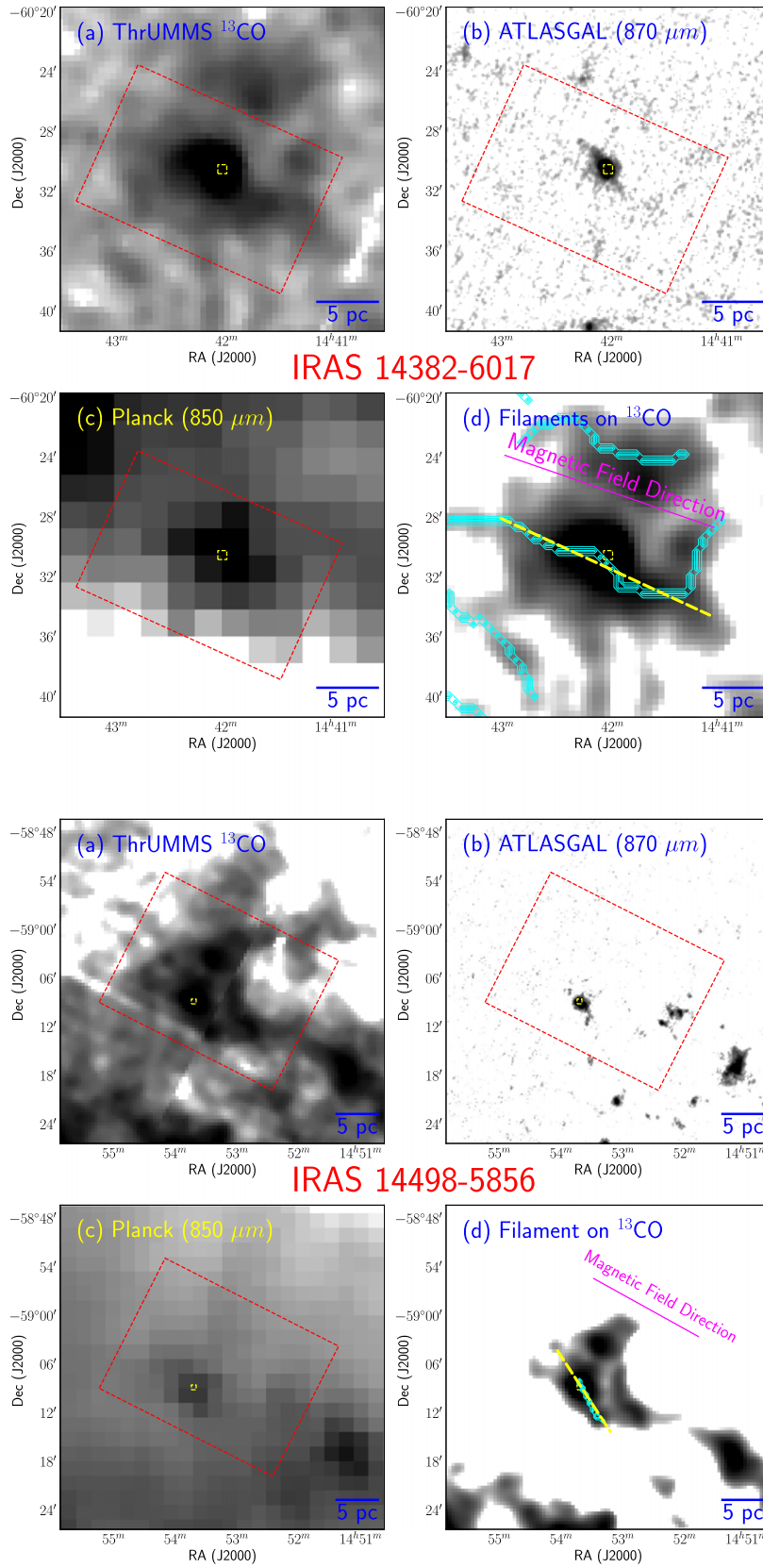
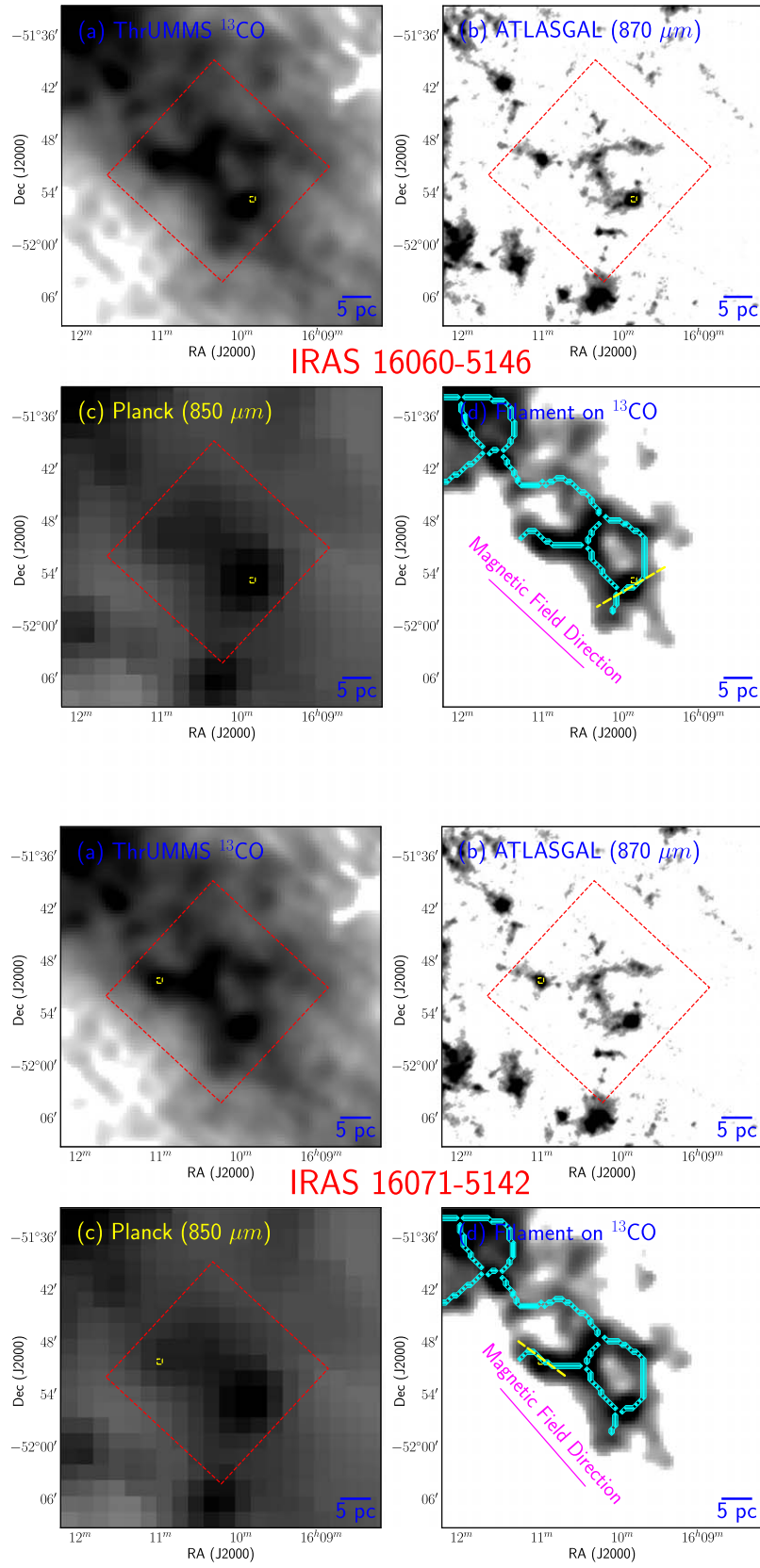
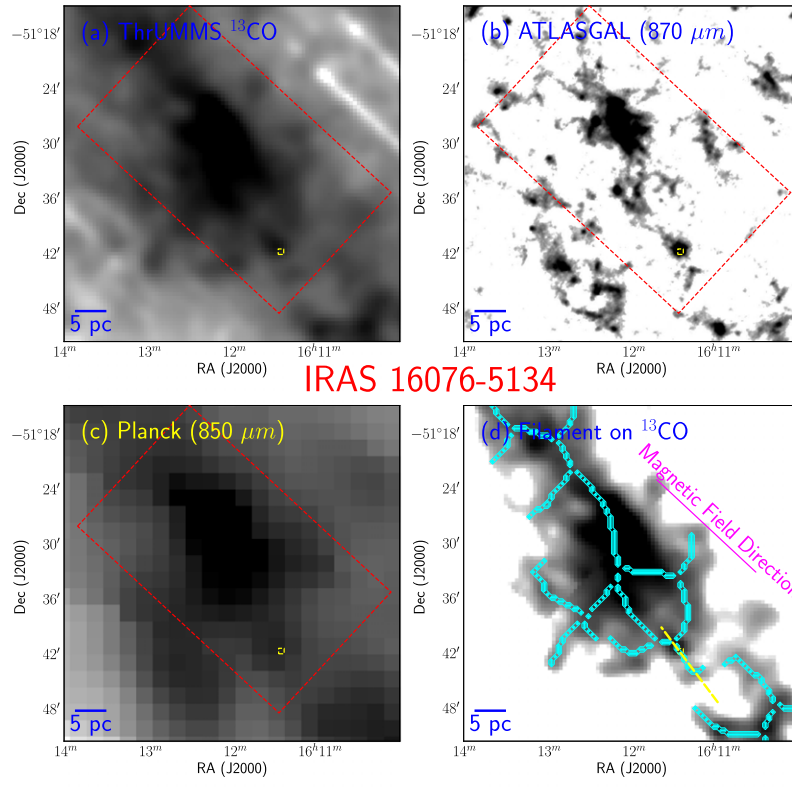


Figure 7. Distribution of gas and dust in the IRAS 14382-6017 the regions associated with filaments (namely, IRAS 14382-6017, IRAS 14498-5856, IRAS 16060-5146, IRAS 16071-5142, IRAS 16076-5134, and IRAS 17220-3609). Filaments are detected in the integrated ^{13}CO and ATLASGAL $870\ \mu\text{m}$ images. The symbols are the same as those in Figure 2.





IRAS 17220-3609

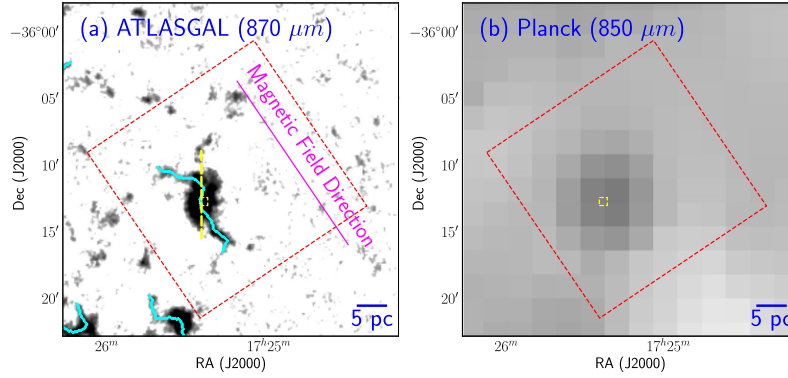


Figure 7. (Continued.)

continuum maps. The Python-based FILFINDER algorithm (Koch & Rosolowsky 2015) was also applied on all the identified molecular clouds to trace the filamentary structures. Two example figures are presented in Figures 2 and 3. Figures corresponding to the rest of the regions are presented here in two sets: sources with filaments are presented in Figure 7 and sources without filaments are presented in Figure 8. Note that ^{13}CO data were not available for the IRAS 17204-3636 and IRAS

17220-3609 regions. Thus, host clouds in these two regions were identified based on the $870\ \mu\text{m}$ ATLASGAL image.

Appendix B Cumulative Distribution of γ_{Fil}

Figure 9 shows the cumulative distribution of γ_{Fil} after adding a random value within the uncertainty limit of $\pm 10^\circ$.

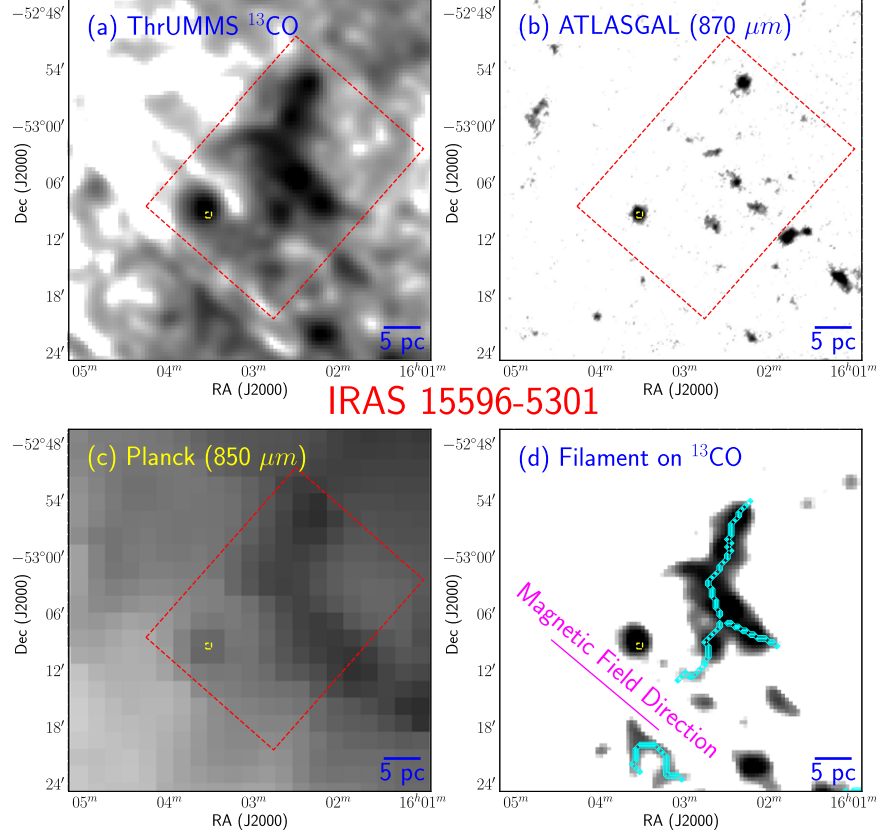


Figure 8. Distribution of gas and dust in the regions where no filamentary structure is detected in the integrated ^{13}CO and ATLASGAL $870\ \mu\text{m}$ images (namely IRAS 15596-5301, IRAS 16272-4837, and IRAS 17204-3636). Symbols are the same as in Figure 2.

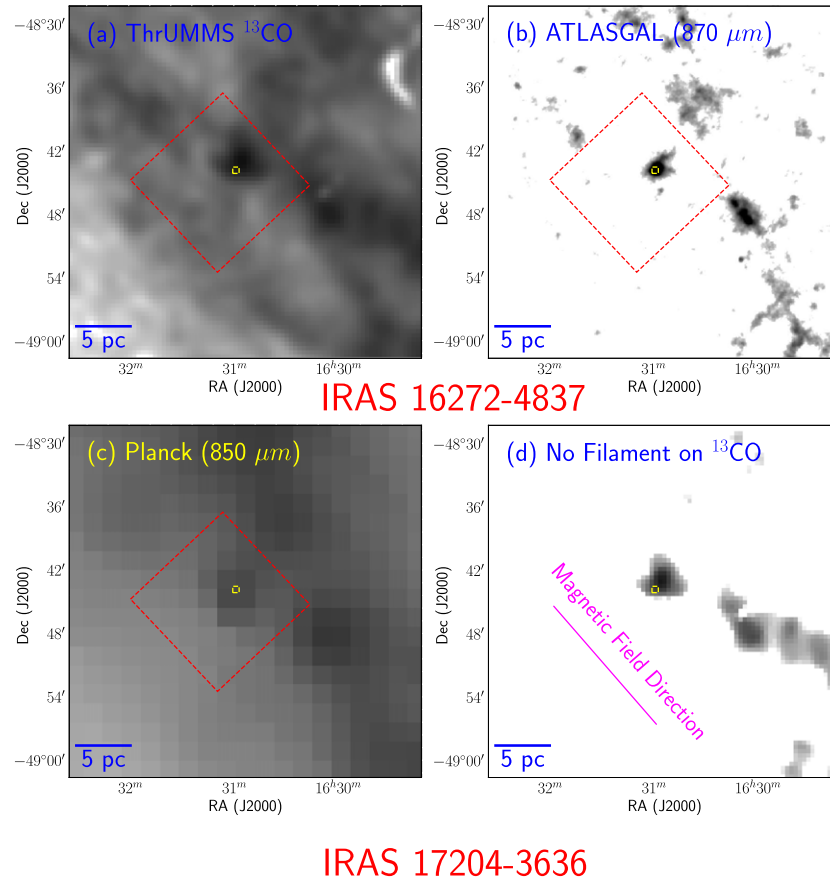
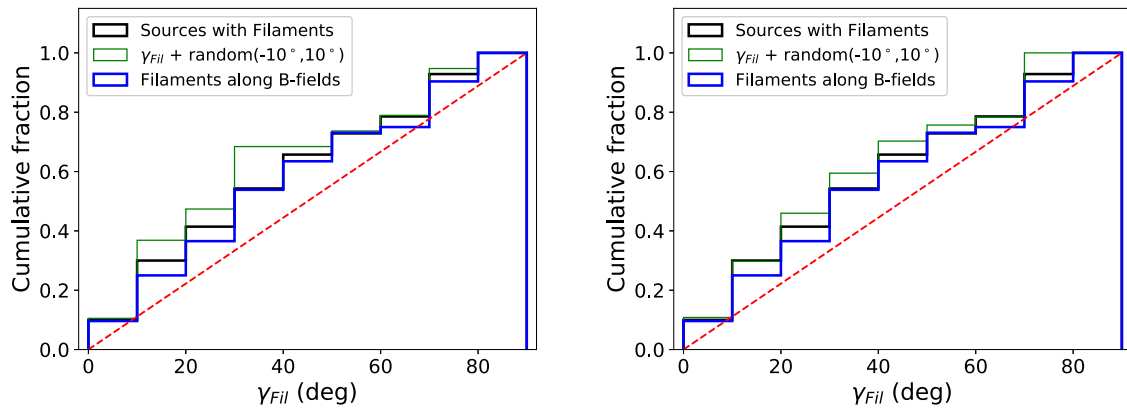



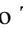




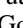



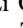
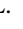


Figure 8. (Continued.)

Figure 9. Two examples of cumulative distribution functions of γ_{Fil} with randomly added values within $\pm 10^\circ$. No significant change is noted in the distribution.

ORCID iDs

T. Baug  <https://orcid.org/0000-0003-0295-6586>
 Ke Wang  <https://orcid.org/0000-0002-7237-3856>
 Tie Liu  <https://orcid.org/0000-0002-5286-2564>
 Mengyao Tang  <https://orcid.org/0000-0001-9160-2944>
 Qizhou Zhang  <https://orcid.org/0000-0003-2384-6589>
 Di Li  <https://orcid.org/0000-0003-3010-7661>
 Chakali Eswaraiah  <https://orcid.org/0000-0003-4761-6139>
 Sheng-Yuan Liu  <https://orcid.org/0000-0003-4603-7119>
 Paul F. Goldsmith  <https://orcid.org/0000-0002-6622-8396>
 Leonardo Bronfman  <https://orcid.org/0000-0002-9574-8454>
 Sheng-Li Qin  <https://orcid.org/0000-0003-2302-0613>
 Viktor L. Tóth  <https://orcid.org/0000-0002-5310-4212>
 Pak-Shing Li  <https://orcid.org/0000-0001-8077-7095>
 Kee-Tae Kim  <https://orcid.org/0000-0003-2412-7092>

References

- Anathpindika, S., & Whitworth, A. P. 2008, *A&A*, **487**, 605
 André, P., Di Francesco, J., Ward-Thompson, D., et al. 2014, in *Protostars and Planets VI*, ed. H. Beuther (Tucson, AZ: Univ. Arizona Press), 27
 André, P., Men'shchikov, A., Bontemps, S., et al. 2010, *A&A*, **518**, L102
 Arce, H. G., Borkin, M. A., Goodman, A. A., et al. 2011, *ApJ*, **742**, 105
 Arzoumanian, D., André, P., Didelon, P., et al. 2011, *A&A*, **529**, L6
 Bally, J. 2016, *ARA&A*, **54**, 491
 Barnes, P. J., Muller, E., Indermühle, B., et al. 2015, *ApJ*, **812**, 6
 Baug, T., Dewangan, L. K., Ojha, D. K., et al. 2018, *ApJ*, **852**, 119
 Bodenheimer, P. 1995, *ARA&A*, **33**, 199
 Busquet, G., Zhang, Q., Palau, A., et al. 2013, *ApJL*, **764**, L26
 Chapman, N. L., Davidson, J. A., Goldsmith, P. F., et al. 2013, *ApJ*, **770**, 151
 Clarke, S. D., Whitworth, A. P., Duarte-Cabral, A., et al. 2017, *MNRAS*, **468**, 2489
 Corradi, R. L. M., Aznar, R., & Mampaso, A. 1998, *MNRAS*, **297**, 617
 Dale, J. E., & Bonnell, I. 2011, *MNRAS*, **414**, 321
 Davis, C. J., Froebrich, D., Stanke, T., et al. 2009, *A&A*, **496**, 153
 Faúndez, S., Bronfman, L., Garay, G., et al. 2004, *A&A*, **426**, 97
 Fernández-López, M., Arce, H. G., Looney, L., et al. 2014, *ApJL*, **790**, L19
 Galametz, M., Maury, A., Girart, J. M., et al. 2018, *A&A*, **616**, A139
 Goodman, A. A., Benson, P. J., Fuller, G. A., et al. 1993, *ApJ*, **406**, 528
 Gray, W. J., McKee, C. F., & Klein, R. I. 2018, *MNRAS*, **473**, 2124
 Hacar, A., Tafalla, M., Kauffmann, J., et al. 2013, *A&A*, **554**, A55
 Hull, C. L. H., Plambeck, R. L., Kwon, W., et al. 2014, *ApJS*, **213**, 13
 Hull, C. L. H., & Zhang, Q. 2019, *FrASS*, **6**, 3
 Kirk, H., Myers, P. C., Bourke, T. L., et al. 2013, *ApJ*, **766**, 115
 Koch, E. W., & Rosolowsky, E. W. 2015, *MNRAS*, **452**, 3435
 Kong, S., Arce, H. G., Maureira, M. J., et al. 2019, *ApJ*, **874**, 104
 Kudoh, T., & Basu, S. 2008, *ApJL*, **679**, L97
 Lee, J. W. Y., Hull, C. L. H., & Offner, S. S. R. 2017, *ApJ*, **834**, 201
 Lee, K. I., Dunham, M. M., Myers, P. C., et al. 2016, *ApJL*, **820**, L2
 Lee, K. I., Fernández-López, M., Storm, S., et al. 2014, *ApJ*, **797**, 76
 Li, H., Li, D., Qian, L., et al. 2015, *ApJS*, **219**, 20
 Li, H.-bai., Fang, M., Henning, T., et al. 2013, *MNRAS*, **436**, 3707
 Li, P. S., & Klein, R. I. 2019, *MNRAS*, **485**, 4509
 Li, P. S., McKee, C. F., & Klein, R. I. 2015, *MNRAS*, **452**, 2500
 Liu, H. B., Jiménez-Serra, I., Ho, P. T. P., et al. 2012, *ApJ*, **756**, 10
 Liu, T., Kim, K.-T., Yoo, H., et al. 2016a, *ApJ*, **829**, 59
 Liu, T., Zhang, Q., Kim, K.-T., et al. 2016b, *ApJ*, **824**, 31
 Lu, X., Zhang, Q., Liu, H. B., et al. 2018, *ApJ*, **855**, 9
 Machida, M. N., Hirano, S., & Kitta, H. 2020, *MNRAS*, **491**, 2180
 Machida, M. N., Matsumoto, T., Hanawa, T., et al. 2005, *MNRAS*, **362**, 382
 Matthews, B. C., & Wilson, C. D. 2000, *ApJ*, **531**, 868
 Myers, P. C. 2009, *ApJ*, **700**, 1609
 Offner, S. S. R., Dunham, M. M., Lee, K. I., et al. 2016, *ApJL*, **827**, L11
 Pineda, J. E., Arce, H. G., Schnee, S., et al. 2011, *ApJ*, **743**, 201
 Pineda, J. E., Offner, S. S. R., Parker, R. J., et al. 2015, *Natur*, **518**, 213
 Planck Collaboration, Adam, R., Ade, P. A. R., et al. 2016a, *A&A*, **594**, A1
 Planck Collaboration, Adam, R., Ade, P. A. R., et al. 2016b, *A&A*, **594**, A8
 Planck Collaboration, Ade, P. A. R., Aghanim, N., et al. 2016c, *A&A*, **586**, A136
 Planck Collaboration, Ade, P. A. R., Aghanim, N., et al. 2016d, *A&A*, **594**, A19
 Reid, M. J., Menten, K. M., Brunthaler, A., et al. 2014, *ApJ*, **783**, 130
 Santos, F. P., Busquet, G., Franco, G. A. P., et al. 2016, *ApJ*, **832**, 186
 Schuller, F., Menten, K. M., Contreras, Y., et al. 2009, *A&A*, **504**, 415
 Siringo, G., Kreysa, E., Kovács, A., et al. 2009, *A&A*, **497**, 945
 Stephens, I. W., Dunham, M. M., Myers, P. C., et al. 2017, *ApJ*, **846**, 16
 Targon, C. G., Rodrigues, C. V., Cerqueira, A. H., et al. 2011, *ApJ*, **743**, 54
 Tatematsu, K., Ohashi, S., Sanhueza, P., et al. 2016, *PASJ*, **68**, 24
 Wang, K., Testi, L., Burkert, A., et al. 2016, *ApJS*, **226**, 9
 Wang, K., Testi, L., Ginsburg, A., et al. 2015, *MNRAS*, **450**, 4043
 Wang, K., Zhang, Q., Wu, Y., et al. 2011, *ApJ*, **735**, 64
 Wang, K., Zhang, Q., Wu, Y., et al. 2012, *ApJL*, **745**, L30
 Wang, Ke. 2018, *RNAAS*, **2**, 52
 Wenger, T. V., Balser, D. S., Anderson, L. D., & Bania, T. M. 2018, *ApJ*, **856**, 52
 Yuan, J., Li, J.-Z., Wu, Y., et al. 2018, *ApJ*, **852**, 12
 Zhang, Q., Qiu, K., Girart, J. M., et al. 2014, *ApJ*, **792**, 116